Research article

Er Pan, Gongxun Bai*, Yutao Peng, Liang Chen and Shiqing Xu*

Promoting luminescence of Yb/Er codoped ferroelectric composite by polarization engineering for optoelectronic applications

https://doi.org/10.1515/nanoph-2019-0230
Received July 29, 2019; revised August 31, 2019; accepted September 3, 2019

Abstract: Ferroelectric oxide nanocrystals, in combination with the robust coupling of an electric field with crystal structure symmetry, makes such systems agreeable to field-induced crystal structural transformation. The luminescent properties of rare earth ions are sensitive to the symmetry of the surrounding crystal field. The luminescence tuning of rare earth ions is an important assignment in the research of luminescent materials. However, the current conditional feasibility and reversibility in the exploration of luminescence modification remain major challenges. In this article, the luminescence modulation of rare earth ions has been developed in Yb^{3+}/Er^{3+} codoped ferroelectrics glass ceramics containing $Bi_4Ti_3O_{12}$ nanocrystals through an electric field. The inclusion of nanocrystals in the glass matrix greatly enhances the electrical resistance. Both upconversion and near-infrared emissions of rare earth ions are effectively enhanced more than twice via polarization engineering. The electric field regulates the photonic properties of rare earth ions with excellent reversibility and nonvolatility in ferroelectrics. The effective modification by electric field provides a new scheme for optical storage and optoelectronic devices.

Keywords: upconversion; near-infrared; modified luminescence; ferroelectrics; polarization.

***Corresponding authors: Gongxun Bai and Shiqing Xu,** Institute of Optoelectronic Materials and Devices, China Jiliang University, Hangzhou 310018, People's Republic of China,
e-mail: baigx@cjlu.edu.cn (G. Bai); shiqingxu@cjlu.edu.cn (S. Xu).
https://orcid.org/0000-0002-4066-0359 (G. Bai)
Er Pan and Yutao Peng: Institute of Optoelectronic Materials and Devices, China Jiliang University, Hangzhou 310018, People's Republic of China
Liang Chen: Institute of Optoelectronic Technology, China Jiliang University, Hangzhou 310018, PR China

1 Introduction

Oxide ferroelectric materials have comprehensive applications in nonvolatile memories, actuators, and capacitors for optoelectronic applications [1, 2]. Ferroelectric nanocrystalline composites belong to optoelectrical composites where ferroelectric crystals are distributed in the glass matrix. Ferroelectric glass ceramics have been used for optoelectronic devices such as phase shifters and tunable filters. Polarization rotation plays an irreplaceable role in the application of ferroelectric materials. In the displacement type ferroelectric, the position of the lowest energy coordinates shifts with the adjustment of the structure, resulting in the rotation of the electric dipole [3–7]. The spatial structure of $Bi_4Ti_3O_{12}$ consists of three perovskite-like units and one fluorite-like unit, which are alternatively stacked in the transverse direction. When the $Bi_4Ti_3O_{12}$ crystal is polarized in an electric field, the polarization of $Bi_4Ti_3O_{12}$ mainly proceeds along the a-axis direction, mainly from the movement of cations relative to O ions within the perovskite block. The $Bi_4Ti_3O_{12}$ single crystal was found to have large spontaneous polarization along the a-axis of 50 μC/cm^2 and a small polarization along the c-axis of 4 μC/cm^2. Among the lead-free ferroelectric materials, the polarizability of Bi^{3+} ions in $Bi_4Ti_3O_{12}$ based ferroelectric materials is second only to the Pb^{2+} group, which is attributed to the $6s^2$ lone pairs [8, 9]. So $Bi_4Ti_3O_{12}$ ferroelectrics will undergo large and structural distortion through external electric field stimulation [10–12]. The external electric field drives the nanoscale shift of the active cations within $Bi_4Ti_3O_{12}$, which effects the crystal structure. If the rare earth ions are doped into the ferroelectric hosts, tuning the ligand field will be possible to realize the luminescence modulation.

Ferroelectric oxide nanocrystals with rare earth ions have great potential in future optoelectronic devices due to their unique luminescence and inherent electric properties. Rare earth ions doped luminescent material have received great attention because of their practical and potential applications, including bioimaging, photodynamic therapy, noncontact sensing, anti-counterfeiting and colorful display

Open Access. © 2019 Gongxun Bai, Shiqing Xu et al., published by De Gruyter. This work is licensed under the Creative Commons Attribution 4.0 Public License.

[13–22]. Rare earth ions have unique and excellent optical properties such as low biotoxicity, low photobleaching, long lifetime, high photostability, large anti-Stokes shifts [23–25]. Modification of the luminescent properties of rare earth ions is important for applications [14, 26–29]. For instance, Professor Hao's team developed the upconversion luminescence enhancement of the rare earth ions doped barium titanate ($BaTiO_3$) ferroelectric thin film through an electric field [30]. Traditional chemical methods are often employed to modify the luminescent properties of rare earth ions, which tailor the composition of the host and the proportion of dopant ions. However, traditional chemical methods are prone to induce changes in uncontrollable parameters such as crystal defects, uneven composition, etc., which hinders the more precise understanding of luminescence tuning of rare earth ions. It is interesting to find in a host that the luminescent properties of rare earth ions can be modulated in the one sample by external stimuli.

In this paper, Yb^{3+}/Er^{3+} codoped oxide ferroelectric composites have been synthesized. As Er^{3+} ions can emit strong upconversion visible and downconversion near-infrared (NIR) emissions under 980 nm excitation. Yb^{3+} ions can efficiently absorb pumping photons under 980 nm excitation and transfer excitation energy to adjacent Er^{3+} ions. Based on the sensitivity of rare earth ions luminescence to crystal field inhomogeneities, Yb^{3+}/Er^{3+} can be employed as luminescent probes to detect the reversible nanoscale bond perturbations of $Bi_4Ti_3O_{12}$ under an electric field. The flexibility of the ferroelectric lattice, and the strong coupling of the crystal structure and polarization, enables the system to achieve reversible transformation of the electric field-induced structure. The reversible structure change of $Bi_4Ti_3O_{12}$ ferroelectric material induced by an electric field can effectively modify Yb^{3+}/Er^{3+} luminescence with nonvolatile. The developed Yb^{3+}/Er^{3+} codoped glass composite containing ferroelectric $Bi_4Ti_3O_{12}$ nanocrystals have wide uses in storage and photonic devices.

2 Experimental procedures

The prepared samples were based on the system of B_2O_3-Bi_2O_3-TiO_2-Al_2O_3, and nanocrystalline composites were prepared with different molar compositions of $48B_2O_3$-$28Bi_2O_3$-$21TiO_2$-$1.5Al_2O_3$-$1Yb_2O_3$-$0.5Er_2O_3$ (mol %), labeled as BTO. Yb^{3+}/Er^{3+} were codoped into the ferroelectric $Bi_4Ti_3O_{12}$ nanocrystalline composite through melt quenching and the heat treatment method. First the raw material (all reagents were bought from Aladdin Industrial Corporation, Shanghai, China) was weighed and thoroughly mixed. Then the raw materials were put into an electric muffle furnace at 1500°C for 40 min. The melt was poured onto a preheated stainless-steel plate. In order to remove the residual stress, the sample was transferred to a furnace at 500°C for 5 h. The obtained was cut into the appropriate size for measurement. And then the ferroelectric nanocrystals were formed in the glass matrix after a suitable heat treatment process. The heat-treated samples were optically polished and for the next test measurement. The measurements of the ferroelectric performance were performed using Radiant Precision Premier II technology (Radiant Technologies Inc., NM, USA). The annealed samples were separated into the uniform square (8×8 mm). The heat treatments of samples were accomplished in the same muffle furnace and then the samples were polished to the thickness of 0.25 mm. After cautious operation, all samples were optically tested to ensure the uniformity of chemical homogeneities. The visible and NIR emission spectra of the samples had unexceptionable consistency. In the ferroelectric test, the low-freezing-point silver paint of which curing temperature was around 80–100°C was coated evenly in the samples. The samples experienced 100°C for 60 min in the drying oven for the solidification of the sliver paint. Subsequently, the ferroelectric characteristic was recorded and varying electrical fields were applied to the samples. The visible and NIR emission performance was measured with the elevation of the electric field.

The crystallization temperature of the sample was measured using a Netzsch DTA 404 PC (DTA 404PC, NETZSCH, Free State of Bavaria, Germany) with a heating rate of 10°C/min. The X-ray diffraction (XRD) analysis pattern was obtained by using a Bruker D2 Phaser diffractometer (D2 PHASER, Bruker, Karlsruhe, Germany) equipped with Cu-Kα radiation. The Raman spectra of Yb^{3+}/Er^{3+} codoped $Bi_4Ti_3O_{12}$ nanocomposite was recorded by using Renishaw inVia Raman microscope spectroscopy (inVia-Reflex, Renishaw, Gloucestershire, UK). The microstructure of the precursor and the $Bi_4Ti_3O_{12}$ composite was characterized by high-resolution transmission electron microscopy (TEM, Tecnai G2 F20, FEI, Hillsboro, OR, USA). The luminescence spectra of Yb^{3+}/Er^{3+} in the amples were recorded using a Jobin-Yvon Fluorolog-3 fluorescence spectrophotometer (Fl-3-211, Jobin Yvon, Paris, France) and a 980 nm laser diode. The hysteresis loops were measured on a ferroelectric test system (Radiant Technologies Inc., NM, USA), and the sample under test was immersed in silicone oil to avoid leakage. All measurements were performed at room temperature.

3 Results and discussion

According to differential thermal analysis, the precursor samples were arranged at 680°C for 3 h for nucleation heat

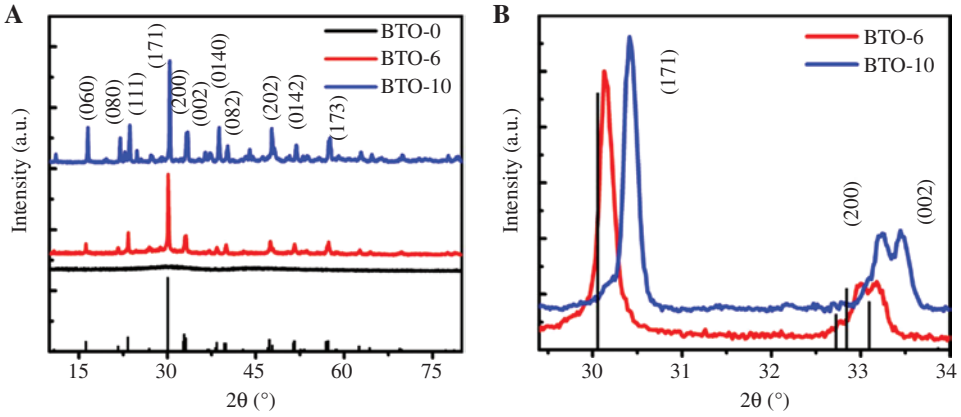

Figure 1: Structural characterization of the prepared samples and ferroelectric composite.
(A) The XRD pattern of BTO-j (j = 0, 6, and 10) samples. (B) The partially amplified XRD patterns of the prepared BTO-j samples.

treatment. And then the samples were reheated by being treated at 760°C for 6 and 10 h, respectively. The samples based on heat treatment time were labeled as BTO-j (j = 0, 6, 10). The XRD results of BTO-j samples are presented in Figure 1A. As shown in Figure 1A, the XRD pattern of the sample BTO-0 has no diffraction peak, indicating that no crystal phase is in the glass matrix. While some stronger diffraction peaks were presented after an additional heat treatment process. The sample diffraction peaks of BTO-6 and BTO-10 match well with standard card PDF#35-0795. It suggests that treatment sample contained the pure $Bi_4Ti_3O_{12}$ crystal phase, and the crystal grain diameter in the BTO-10 sample can be calculated using the Scherrer formula to be about 10 nm. It can be extracted from Figure 1A that the diffraction peaks of BTO-6 and BTO-10 are significantly shifted to the right when compared to the standard card. A partial enlargement of the position from 29.3 to 34.2 degrees is shown in Figure 1B. Compared to the standard peak position, the diffraction peaks (171), (200) and (002) of BTE-6 and BTE-10 are all shifted to a large angle. The 2θ of the (171) plane in BTO-0 and BTO-10, respectively, are 30.057 and 30.4123. The diffraction peak of crystal plane (171) in BTE-10 is shifted by an angle of 0.355 degrees compared to the standard card. According to the Bragg equation, the interplanar (171) spacing of $Bi_4Ti_3O_{12}$ reduced 0.034 Å after heat treatment for 10 h. The right shifting indicates that the lattice of $Bi_4Ti_3O_{12}$ shrinks, which can be attributed to the introduction of Yb^{3+}/Er^{3+} ions into the crystal lattice. As the charge number of Yb^{3+}/Er^{3+} is the same as that of Bi^{3+}, and the cation radius of Yb^{3+} (0.0868 nm) and Er^{3+}(0.089 nm) is closer to Bi^{3+} (0.103 nm) than Ti^{4+} (0.0605 nm). Therefore, the result of Figure 2A may originate from the fact that the Yb^{3+}/Er^{3+} ion preferentially replaces the Bi^{3+} ions, causing the disordered lattice. In addition, the shift of BTO-10 is significantly greater than that of BTO-6, which indicates that BTO-10 has more Yb^{3+}/Er^{3+} in the $Bi_4Ti_3O_{12}$ unit cell.

Figure 2A and B show the HR-TEM image of BTO-10. Figure 2A intuitively demonstrates that the diameter of the nanocrystals in the sample is approximately 10 nm, and around the crystals is an amorphous glass matrix. Figure 2B shows that the interplanar spacing d is 0.276 nm, which is assigned to the (002) crystal plane of the $Bi_4Ti_3O_{12}$ crystal. The Raman spectra of BEO-0 and BTO-10 are shown in Figure 2C. The transformation in the Raman spectra was apparent after crystallization. By comparing the related cases of $BaTiO_3$ and $PbTiO_3$ crystals [31, 32], the Raman modes at 300, 361, 402, 441, and 823 cm^{-1} are originated from the stretching or bending vibration of Ti-O. The modes around 538 and 578 cm^{-1} are attributed to the displacement of the external oxygen atoms of the TiO_6 octahedron. The Raman peaks around 90 cm^{-1} is considered to be related to the vibration of Bi^{3+} ions. In the precursor sample, there is an amorphous matrix without an obvious Raman reflection mode. The lattice vibrations of $Bi_4Ti_3O_{12}$ crystals appeared after the heat treatment. The XRD Raman results indicate that nanocrystals $Bi_4Ti_3O_{12}$ are incorporated into the glass matrix. $Bi_4Ti_3O_{12}$ is a well-known displacement type ferroelectric. The ferroelectric research results are shown in Figure 2D, which shows that the polarization performance in the BTO-10 sample gradually increases with the elevated electric field. Samples were loaded with pulse voltages of 30, 60, 90, and 120 kV/cm, recorded as EF-i (i = 0, 30, 60, 90, 120). When the electric field is raised to a critical value, the value of the breakdown electric field is 136 kV/cm. The $Bi_4Ti_3O_{12}$ structure preserves varying degrees of remnant polarization, insinuating a distortion of the $Bi_4Ti_3O_{12}$ structure and a decrease in the symmetry of the crystal field. The remanent polarization of the EF-i sample increases with increasing electric field, and the remanent polarization of EF-120 is increased by 13.2 times compared to EF-30. The remanent polarization has a significant retention in the ferroelectrics, which

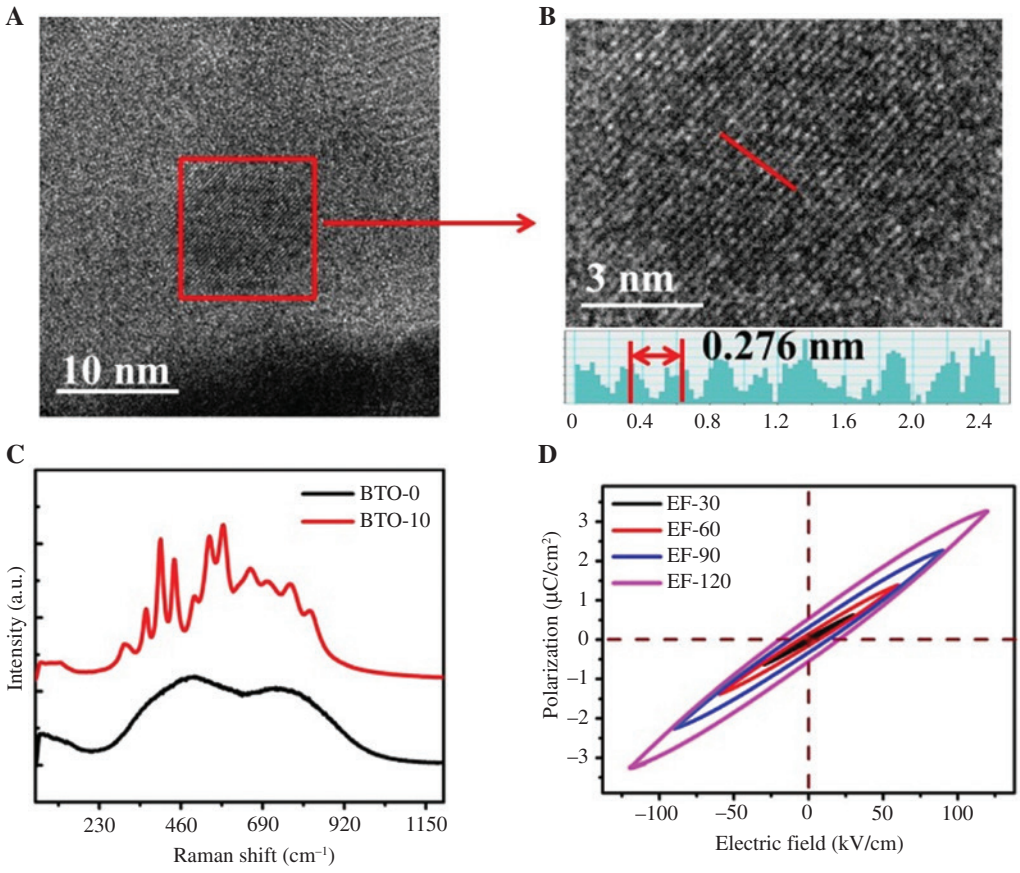

Figure 2: Crystal's morphology and ferroelectric properties of the ferroelectric composite.
(A) The HR-TEM image of BTO-10. (B) The HR-TEM image of the nanocrystal and lattice. (C) Raman spectra of BTO-0 and BTO-10 samples. (D) Ferroelectric hysteresis P-E loop of EF-i (i = 0, 30, 60, 90 and 120).

implies that the difference in lattice deformation of EF-i is significant.

Luminescence results for samples with the elevation of electric fields are presented in Figure 3. As shown in Figure 3A and B, the upconversion luminescence of the Er^{3+} ions is remarkably enhanced. The luminescence intensity of the Er^{3+}:$^2H_{11/2}$-$^4I_{15/2}$, $^4S_{3/2}$-$^4I_{15/2}$ and $^4F_{9/2}$-$^4I_{15/2}$ transitions increases by 2.04, 2.05, 2.28 times, respectively. The NIR fluorescence spectra of Er^{3+} ion are presented in Figure 3C, it is found that the NIR luminescence at 1.54 μm of Er^{3+}:$^4I_{13/2}$-$^4I_{15/2}$ transition is effectively enhanced by 2.66 times. The probability of corresponding energy level transitions increases, which results in a significant modification of the visible and NIR luminescence of Er^{3+} ions. The sensitivity of rare earth ions to crystal field symmetry plays a crucial role in electric field modified luminescence. This mechanism is discussed in Figure 3. Figure 3D shows the energy transition diagram. Yb^{3+} has only one excited state level and it has a strong and broad absorption band around 980 nm. There is a perfect resonance between the Yb^{3+}:$^2F_{5/2}$ and Er^{3+}:$^4I_{11/2}$ energy levels, so there is an effective energy transfer from Yb^{3+} to Er^{3+} ions. The ground state level Er^{3+}:$^4I_{15/2}$ is excited to the Er^{3+}:$^4I_{11/2}$ level by the excited state absorption or energy transfer process from the adjacent Yb^{3+} ions. Some excited state populations of the Er^{3+}:$^4I_{11/2}$ level is non-radiation attenuated and filled to the Er^{3+}:$^4I_{13/2}$ levels. The other excited population of the Er^{3+}:$^4I_{11/2}$ level absorbs the excitation radiation through the excited state absorption process and transits to the Er^{3+}:$^4F_{7/2}$ excited state level. The excited state of the Er^{3+}:$^4F_{7/2}$ level has nonradiation attenuation to the $^2H_{11/2}$ and $^4S_{3/2}$ levels in Er^{3+}, and then the Er^{3+}:$^2H_{11/2}$-$^4I_{15/2}$ and $^4S_{3/2}$-$^4I_{15/2}$ transitions lead to green emissions at 531 and 554 nm, respectively. The population of the Er^{3+}:$^4I_{13/2}$ level absorbs the photon transition to the Er^{3+}:$^4F_{9/2}$ level. Er^{3+}:$^4F_{9/2}$-$^4I_{15/2}$ and $^4I_{13/2}$-$^4I_{15/2}$ radiation transitions result in emission bands at 656 and 1540 nm, respectively.

The enhancement factors of the upconversion and NIR luminescence in the samples after loading different electric fields are presented in Figure 4A. It is found that the enhancement factors versus the electric field strength show a nearly linear relationship. The structure results

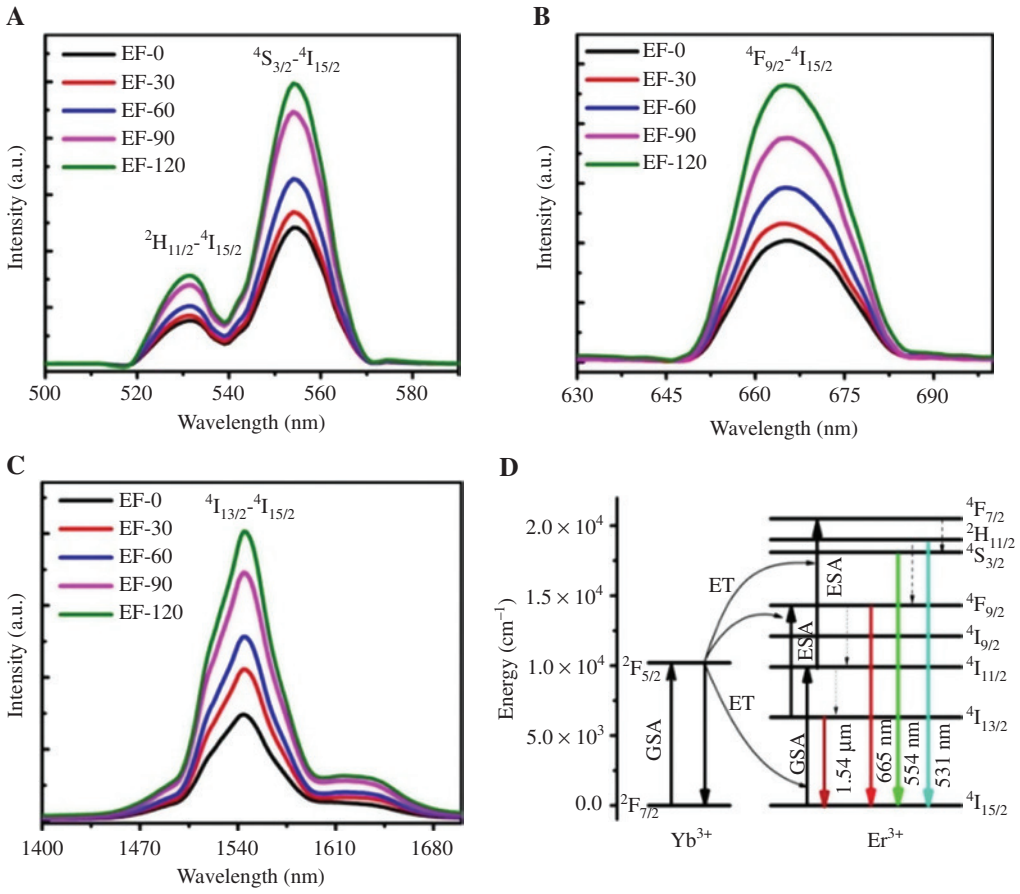

Figure 3: The electric-induced enhancements of visible and near-infrared emission, and schematic diagram of the energy levels. (A) The upconversion emission spectra of Er^{3+}:$^2H_{11/2}$-$^4I_{15/2}$ and $^4S_{3/2}$-$^4I_{15/2}$ transitions with increasing electric fields. (B) The upconversion emission spectra of Er^{3+}:$^4F_{9/2}$-$^4I_{15/2}$ transition with elevated electric fields. (C) The NIR emission of Yb^{3+}/Er^{3+} doped samples with different electric fields. (D) Schematic diagram of the energy levels of Yb^{3+}/Er^{3+} in the nanocomposites.

with different electric fields are shown in Figure 4B–D. Figure 4B shows the XRD patterns of EF-i samples. XRD peaks have an apparent shift to the right with an increased electric field. The partial enlarged view of Figure 4B is presented in Figure 4C. The diffraction peak of crystal plane (171) shifts to a larger angle. The EF-120 shift reaches 0.12 degrees compared with the EF-0. According to the Bragg equation, the plane spacing d(171) of P-0 and p-200 is calculated to be 2.935 and 2.947 Å, respectively. Therefore, the plane spacing of $Bi_4Ti_3O_{12}$ is reduced by 0.012 Å after the applied electric field. This phenomenon indicates that the picoscale displacement of the active ions is driven by the electric field. The displacement of the active ions causes the lattice distortion and the crystal field change around the luminescent ions, resulting in enhanced luminescence. In addition, under and after an applied electric field, the domains of the ferroelectric crystallites exhibit orientation polarization. The orientation polarization also implies that the lattice is distorted via the electric field in the ferroelectric domain. The symmetry of crystal field around rare earth ions is modified, which can affect the rare earth ions physical performance, like luminescence. The Raman spectra of the EF-i samples are presented in Figure 4D. The Raman mode at 538 and 578 cm^{-1} are attributed to the reverse shift of the oxygen atom on the exterior vertices of the TiO_6 octahedron. The mode at 829 cm^{-1} is attributed to the elastic vibration of the symmetrical T-O bond. The Raman spectra of $Bi_4Ti_3O_{12}$ show that the sharp peaks at 538, 583, 829 cm^{-1} shift to the smaller wavenumber, suggesting the enhanced vibration frequency. It is summarized that the shortening of Ti-O bond causes the strengthening of the vibration frequency by the electric field. The phonon energy of the EF-i samples is gradually reduced. In addition, considering the XRD patterns, the picoscale displacement of the cation along the c-axis is driven by a pulsed electric field, and the remanent polarization is retained in the samples. The lower positional symmetry of the doped ions means that the crystal field components are less uniform, which can mix the opposite parity into the 4*f* configuration level.

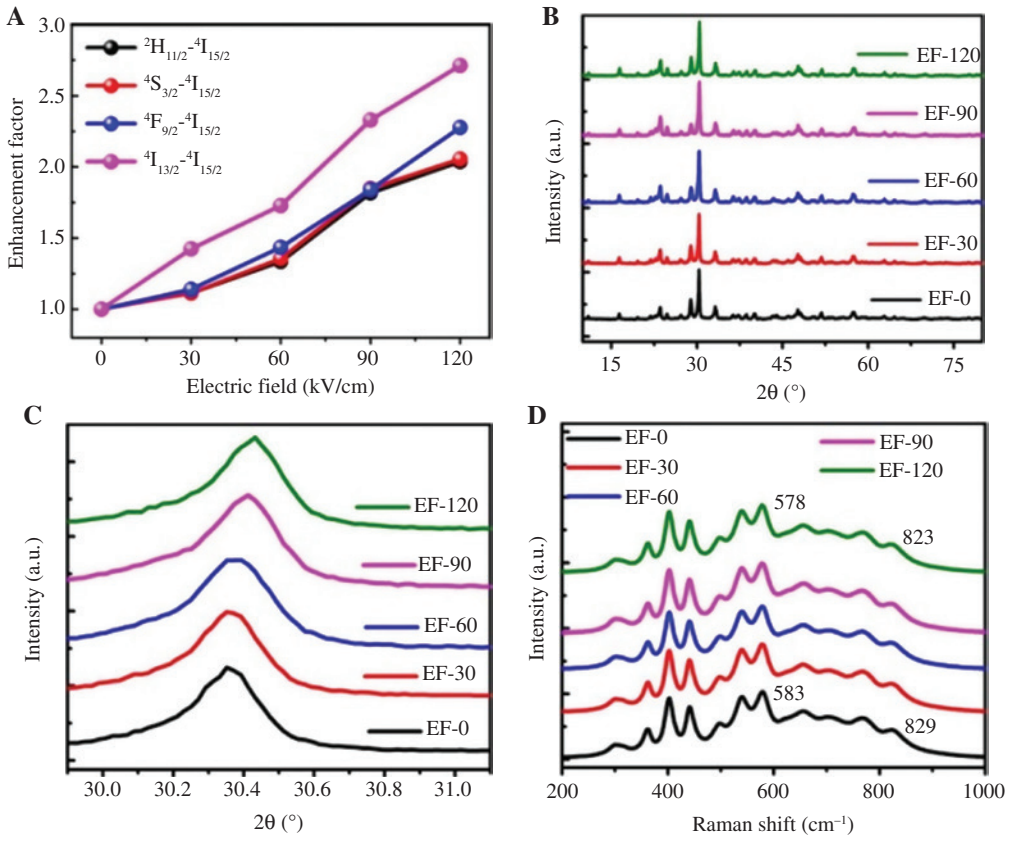

Figure 4: The enhancement of the emission factor, and the change in crystal structural characteristics after the polarization engineering. (A) The relationship between the enhancement factor and the electric field intensity. (B) The XRD patterns of the prepared samples after loading different electric fields. (C) Partially amplified XRD patterns of the prepared samples after loading different electric fields. (D) The Raman spectra of the prepared samples after loading different electric fields.

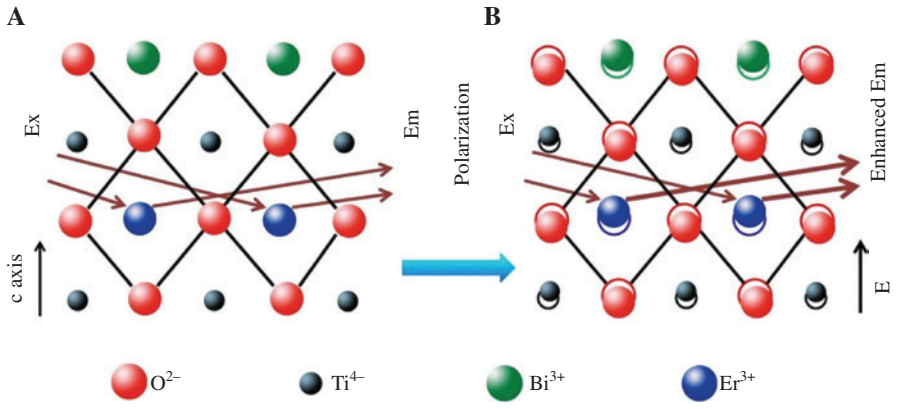

Figure 5: Schematic illustrations for changes of crystal structural characteristics before and after loading the electric field. (A) The bismuth layer structure diagram of $Bi_4Ti_3O_{12}$ is before the loading of the electric field. (B) The bismuth layer structure diagram of $Bi_4Ti_3O_{12}$ is loaded after the electric field is applied.

The promotion in the probability of radiation transition is caused by the displacement of active ions with the elevation of electric field. The probability of radiation transition results in a modulation in luminescence. Meanwhile, the shortening of the T-O bond causes the smaller phonon energy. The relationship between the nonradiation relaxation of Er^{3+} ions and the phonon energy can be expressed by equation:

$$W = W_{NR}(0)[1-\exp(-hw/kT)]^{-\Delta E/hw}$$

$W_{NR}(0)$ represents nonradiative relaxation at 0 K. When the phonon energy becomes lower, the nonradiative transition decreases. Therefore, the energy level transition involves more energy, loading to an effective modification of the luminescence.

In order to explain more deeply the potential physical process of electric field enhancing luminescence of rare earth ions, Figure 5 presents a lattice diagram of Er^{3+} doped $Bi_4Ti_3O_{12}$. In this experiment, a typical bismuth structure ferroelectric $Bi_4Ti_3O_{12}$ is employed. The crystal structure of $Bi_4Ti_3O_{12}$ is alternately arranged over two sublayers of perovskite-like and fluorine-like units along the c-axis, with the number of perovskite-like layers n = 3. In the previous measurement, Er^{3+} tends to replace Bi^{3+} ions. Even in the absence of an applied electric field, Er^{3+} is in an asymmetric crystal field (Figure 5A). When an electric field is applied to the sample, the active cation of the $Bi_4Ti_3O_{12}$ crystal undergoes a pico-scale motion along the c-axis, and the anion shifts in the opposite direction of the c-axis, resulting in the c-axis elongation of the crystal lattice and promotes the asymmetry of the $Bi_4Ti_3O_{12}$ structure (Figure 5B). The lower positional symmetry of the rare earth ions means the more uneven the crystal field components are, which can cause the opposite parity to be mixed into the 4*f* configuration levels and increases the energy levels transition probability of activated ions. Therefore, the active cations and anions are reversely shifted by the electric field, resulting in a greater probability of Er^{3+} radiation transition, which may be a possible mode of the enhanced emission of Er^{3+} ions. The Judd-Ofelt (J-O) theory can deepen the understanding of this modulation mechanism [30]. The J-O theory is derived from the static crystal field mix opposite the parity states. The spontaneous emission probability of rare earth ions can be deduced. It is used to quantitatively estimate the luminescence parameters of rare earth ions within a certain precision. Referring to the J-O theoretical model, the spontaneous emission probability A_{ed} for energy transfer process between initial J manifold and a final J manifold is:

$$A_{ed} = \frac{64\pi^4 e^2}{3h(2j+1)\lambda^3}\left[\frac{n(n^2+2)^2}{9}\right]S_{ed}$$

where n is the refractive index of the sample, h is the Plank constant, e is the electron charge, and λ is the center peak

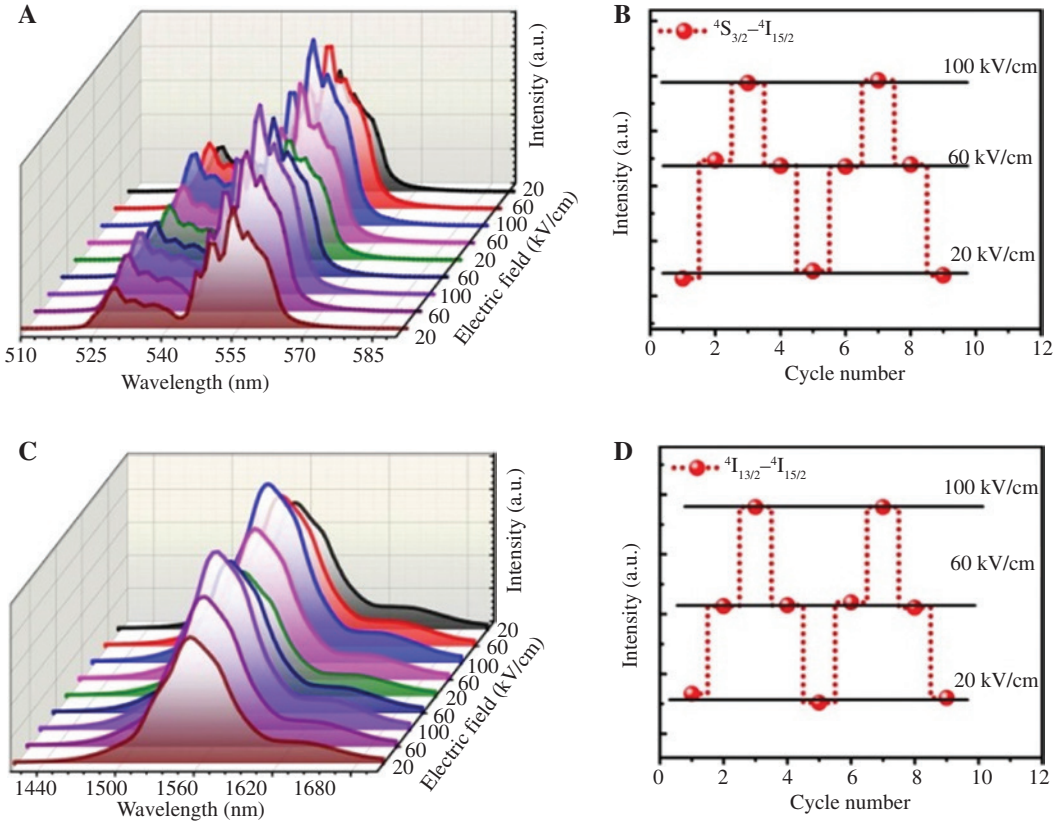

Figure 6: Non-volatile testing of electric field modified luminescence.
(A) The upconversion emission spectra of one sample after pulsed electric fields. (B) Plots of upconversion emission intensity versus a circulating electric field. (C) The NIR luminescence spectra of one sample after loading pulsed electric fields. (D) Plots of NIR emission intensity versus a circulating electric field.

wavelength of the absorption band. The line strength S_{ed} of the electric dipole transition is:

$$S_{ed} = \sum_{t=2,4,6} \Omega_t \left| \langle 4f^n[S, L]J \| U^{(t)} \| 4f^n \| [S', L']J' \rangle \right|^2$$

The Ω_t ($t=2$, 4, and 6) is the intensity parameter, independent of J, which depends on the character of the ligand field. It is a reduced matrix element that does not substantially change with the matrix. Ω_t is contributed to the change in the crystal field around the rare earth ions, and the larger Ω_2 represents a higher crystal field asymmetry. In this experiment, the large enhancement factors of the $^2H_{11/2}$-$^4I_{15/2}$, $^4S_{3/2}$-$^4I_{15/2}$, $^4F_{9/2}$-$^4I_{15/2}$ and $^4I_{13/2}$-$^4I_{15/2}$ transitions of Er^{3+} are shown in Figure 4A. Ω_2 becomes larger due to the lower crystal field symmetry around the Er^{3+} ions. It is concluded that the nanoscale displacement of the active ions in the $Bi_4Ti_3O_{12}$ ferroelectric crystallites occurs after the application of the electric field. The lower crystal field symmetry of the rare earth ions leads to the luminescent modification of the rare earth ions.

Based on these results, it is expected to nonvolatilely modulate the emission of the Yb^{3+}/Er^{3+} by the electric field induced $Bi_4Ti_3O_{12}$ nanocrystalline composite reversible structural transforms. Our luminescent modification may have a good potential application prospect. In particular, nonvolatility and reversibility play an important role in potential applications [33, 34]. The nonvolatile and reversible research presented in Figure 6A and B shows the dependence of the visible green and NIR emission intensities on the electric field. The luminescence intensity of the sample has excellent compliance with changes in the electric field strength. It is demonstrated that the luminescent modification has excellent nonvolatility and reversibility by the electric field. The active ions undergo a shift along the c-axis after loading the electric field. The dependence of the luminescence intensity on the loading voltage is shown in Figure 6B and D. After repeated voltage loadings of 9 times, the transitions of $^4S_{3/2}$-$^4I_{15/2}$ and $^4I_{13/2}$-$^4I_{15/2}$ still maintain superb repeatability. As the structural transformation of ferroelectrics is reversible with the electric field, the electric field modifies the luminescence intensity of rare earth ions, which provides a new solution for the development of optical modulators, anti-counterfeiting, and optical memory.

4 Conclusion

In this work, a novel Yb^{3+}/Er^{3+} codoped nanocomposite material with ferroelectrics properties has been developed. Through an external electric field, Er^{3+}:$^2H_{11/2}$-$^4I_{15/2}$, $^4S_{3/2}$-$^4I_{15/2}$, $^4F_{9/2}$-$^4I_{15/2}$ and $^4I_{13/2}$-$^4I_{15/2}$ transitions were effectively enhanced more than twice. The modulation is reversible and nonvolatile in samples with the same composition. The modification method of Yb^{3+}/Er^{3+} luminescence is different from the conventional routes, such as changing the composition and temperature. The observed phenomenon can be attributed to the picoscale displacement of the crystal field around Er^{3+}, leading to the increased radiation transition probability by an electric field. These results will contribute to further investigate the wide applications of luminescent ferroelectric materials, as this work provides an additional solution for the design of optoelectronic functional devices.

Acknowledgment: This work was financed by the National Natural Science Foundation of China (Grant Nos. 61705214, 61775203, Funder Id: http://dx.doi.org/10.13039/501100001809), the National Key Research and Development Project (Grant No. 2017YFF0210800).

Conflicts of interest: There are no conflicts to declare.

References

[1] Jiang J, Bai ZL, Chen ZH, et al. Temporary formation of highly conducting domain walls for non-destructive read-out of ferroelectric domain-wall resistance switching memories. Nat Mater 2018;17:49–56.
[2] Zhao D, Lenz T, Gelinck G H, et al. Depolarization of multidomain ferroelectric Materials. Nat Commun 2019;10:2547–58.
[3] Bai Y, Vats G, Seidel J, Jantunen H, Juuti J. Boosting photovoltaic output of ferroelectric ceramics by optoelectric control of domains. Adv Mater 2018;30:1803821–29.
[4] Thong HC, Zhao C, Zhou Z, et al. Technology transfer of lead-free (K, Na) NbO_3-based piezoelectric ceramics. Mater Today 2019; DOI: 10.1016/j.mattod.2019.04.016.
[5] Krogstad MJ, Gehring PM, Rosenkranz S, et al. The relation of local order to material properties in relaxor ferroelectrics. Nat Mater 2018;17:718–26.
[6] Zhang Y, Jie W, Chen P, et al. Ferroelectric and piezoelectric effects on the optical process in advanced materials and devices. Adv Mater 2018;30:1707007–42.
[7] Wang K, Malič B, Wu J. Shifting the phase boundary: potassium sodium niobate derivates. MRS Bull 2018;43:607–11.
[8] Co K. Sun FC, Alpay SP, et al. Polarization rotation in $Bi_4Ti_3O_{12}$ by isovalent doping at the fluorite sublattice. Phys Rev B 2019;99:014101–10.
[9] Wisniewski W, Slavov S, Russel C, et al. Growing oriented layers of $Bi_4Ti_3O_{12}$ in $Bi_2O_3/TiO_2/SiO_2/Nd_2O_3/Al_2O_3$ glass-ceramics by melt quenching. Sci Rep 2018;8:8639–50.
[10] Tu S, Huang H, Zhang T, et al. Controllable synthesis of multi-responsive ferroelectric layered perovskite-like $Bi_4Ti_3O_{12}$: photocatalysis and piezoelectric-catalysis and mechanism insight. Appl Catal B-Environ 2017;219:550–62.

[11] Khatua DK, Kalaskar A, Ranjan R. Tuning photoluminescence response by electric field in electrically soft ferroelectrics. Phys Rev Lett 2016;116:117601–6.
[12] Li K, Luo L, Zhang Y, et al. The upconversion luminescence modulation and its enhancement in Er^{3+}-doped $Na_{0.5}Bi_{0.5}TiO_3$ based on photochromic reaction. ACS Appl Mater Inter 2018;10:41525–34.
[13] Wang L, Dong H, Li Y, et al. A new cubic phase for a $NaYF_4$ host matrix offering high upconversion luminescence efficiency. Adv Mater 2015;27:2065–9.
[14] Davis NJLK, Allardice JR, Xiao J, et al. Improving the photoluminescence quantum yields of quantum dot films through a donor/acceptor system for near-IR LEDs. Mater Horiz 2019;6:137–43.
[15] Xia Z, Liu Q. Progress in discovery and structural design of color conversion phosphors for LEDs. Prog Mater Sci 2016;84:59–117.
[16] Pan E, Bai G, Zhou J, et al. Exceptional modulation of upconversion and downconversion near-infrared luminescence in Tm/Yb Codoped ferroelectric nanocomposite by nanoscale engineering. Nanoscale 2019;11:11642–8.
[17] Fang M, Huang S, Li D, et al. Stretchable and self-healable organometal halide perovskite nanocrystal-embedded polymer gels with enhanced luminescence stability. Nanophotonics 2018;7:1949–58.
[18] Bai G, Tsang MK, Hao J. Luminescent ions in advanced composite materials for multifunctional applications. Adv Funct Mater 2016;26:6330–50.
[19] Gao G, Busko D, Kauffmann SW, et al. Wide-range non-contact fluorescence intensity ratio thermometer based on Yb^{3+}/Nd^{3+} co-doped La_2O_3 microcrystals operating from 290 to 1230 K. J Mater Chem C 2018;6:4163–70.
[20] Zhou J, Wen S, Liao J, et al. Activation of the surface dark-layer to enhance upconversion in a thermal field. Nat Photonics 2018;12:154–8.
[21] Lin H, Hu T, Huang Q, et al. Non-rare-earth $K_2XF_7:Mn^{4+}$(X = Ta, Nb): a highly-efficient narrow-band red phosphor enabling the application in wide-color-gamut LCD. Laser Photon Rev 2017;11:1700148–58.
[22] Lu L, Tu D, Liu Y, et al. Ultrasensitive detection of cancer biomarker microRNA by amplification of fluorescence of lanthanide nanoprobes. Nano Res 2017;11:264–73.
[23] Wang Y, Zheng K, Song S, et al. Remote manipulation of upconversion luminescence. Chem Soc Rev 2018;47:6473–85.
[24] Pan E, Bai G, Lei L, et al. The electrical enhancement and reversible manipulation of near-infrared luminescence in Nd doped ferroelectric nanocomposites for optical switches. J Mater Chem C 2019;7:4320–5.
[25] Pan Y, Xie X, Huang Q, et al. Inherently Eu^{2+}/Eu^{3+} Codoped Sc_2O_3 nanoparticles as high-performance nanothermometers. Adv Mater 2018;30:e1705256–172.
[26] Cheng Y, Wang J, Qiu Z, et al. Addressable and color-tunable piezophotonic light-emitting stripes. Adv Mater 2017;29:e1703900–7.
[27] Qian X, Cai Z, Su M, et al. Printable skin-driven mechanoluminescence devices via nanodoped matrix modification. Adv Mater 2018;30:e1800291–9.
[28] Wang L, Li X, Li Z, et al. A new cubic phase for a $NaYF_4$ host matrix offering high upconversion luminescence efficiency. Adv Mater 2015;27:5528–33.
[29] Wong MC, Chen L, Tsang MK, et al. Magnetic-induced luminescence from flexible composite laminates by coupling magnetic field to piezophotonic effect. Adv Mater 2015;27:4488–95.
[30] Hao J, Zhang Y, Wei X. Electric-induced enhancement and modulation of upconversion photoluminescence in epitaxial BaTiO3:Yb/Er thin films. Angew Chem Int Ed 2011;50:6876–80.
[31] Du YL, Zhang MS, Chen Q, et al. Investigation of size-driven phase transition in bismuth titanate nanocrystals by Raman spectroscopy. Appl Phys A-Mater 2003;76:1099–103.
[32] Wederni MA, Kraiem S, Mnassri R, et al. Ytterbium doping effects on structural, optical and electrical properties of $Bi_4Ti_3O_{12}$ system. Ceram Int 2018;44:21893–901.
[33] Zheng M, Sun H, Chan MK, et al. Reversible and nonvolatile tuning of photoluminescence response by electric field for reconfigurable luminescent memory devices. Nano Energy 2019;55:22–8.
[34] Zhang JC, Pan C, Zhu YF, et al. Achieving thermo-mechano-opto-responsive bitemporal colorful luminescence via multiplexing of dual lanthanides in piezoelectric particles and its multidimensional anticounterfeiting. Adv Mater 2018;30:e1804644–53.